ACS Sustainable Chemistry & Engineering

pubs.acs.org/journal/ascecg

Research Article

Electrochemical Dealloying of Ni-Rich Pt−Ni Nanoparticle Network for Robust Oxygen-Reduction Electrocatalysts

Jaeyoung Yoo,[#] Youngtae Park,[#] Jungwoo Choi, Jeonghan Roh, Kihyun Shin, Hyun-Seok Cho, EunAe Cho, Changsoo Lee,* and Hyuck Mo Lee*

Cite This: https://doi.org/10.1021/acssuschemeng.3c04866

Read Online

ACCESS | Metrics & More | Article Recommendations | Supporting Information

ABSTRACT: Increasing the electrochemically active surface area (ECSA) and alloying Pt with transition metals (TMs) are well-known strategies for enhancing the oxygen reduction reaction (ORR) catalytic activities. Herein, we introduce a strategy to produce highly active ORR electrocatalysts with a large ECSA using an electrochemical dealloying process involving leaching of Ni from a Ni-rich Pt−Ni nanoparticle network. The dealloying process yielded a dealloyed Pt−Ni nanoparticle network with rugged surfaces from the Ni-rich Pt−Ni nanoparticle network, resulting in a large ECSA. We also increased the mass activity and utilization efficiency of Pt by modulating the interactions between Pt and Ni. The dealloyed nanoparticle network exhibited a high ORR mass activity, six times higher than that of commercial Pt/C. Moreover, the dealloyed Pt−Ni nanoparticle network exhibited better catalytic stability than the Pt/C after 10000 potential cycles, even without carbon support. The reduced binding energy of the O intermediate due to the effects of Ni (ligand and strain effects) enhanced the ORR activity of the dealloyed nanoparticle network, according to the results of a mechanistic study performed using density functional theory. This study opens new avenues for designing TM-alloy catalysts with high ORR activity for various applications.

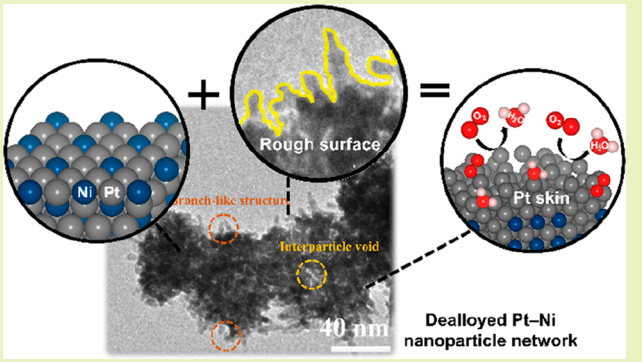

KEYWORDS: *alloy catalyst, catalytic stability, electrochemically active surface area, Ni leaching, Pt/transition metal alloy*

INTRODUCTION

Proton Exchange Membrane Fuel Cells (PEMFCs) are an advanced and sustainable energy technology that has the potential to revolutionize the way we power our world. One of the key advantages of PEMFCs is their ability to use renewable energy sources, such as hydrogen produced from renewable sources such as wind, solar, or hydroelectric power. However, the sluggish cathode reaction rate of PEMFCs could limit their performances. To address this issue, Pt has acted as a state of art electrocatalyst because of its high electrochemical activity, but it still has limitations of high cost and poor durability.[1] Therefore, researchers have developed alternative catalysts that show inexpensive and high-performance ORR. For example, Pt-based alloys with other transition metals (TMs, Pt−X; X = Ni, Co, Fe, and Cu) exhibit higher Pt mass activity for ORR than commercial Pt/C.[2−5] The alloy strategy can reduce the amount of materials needed to generate the same amount of power, which can improve the sustainability of the technology. Researchers are also exploring additional ways to further improve the activity and stability of catalysts through structural design, doping, and surface modification.[6] Overall, the development of highly active Pt-based alloys can lead to a more sustainable and environmentally friendly energy source through reducing the reliance on scarce and expensive materials and increasing the efficiency of PEMFCs.

The improved catalytic activity of Pt-based TM alloys is attributed to ligand and strain effects. The ligand effect is a charge-transfer-induced modulation of the electronic structure due to a difference in electronegativities. In the strain effect, which is a geometric effect, the surface structure is changed owing to the surficial forces that arise from the difference between the atomic radii of Pt and the TM.[7−10] According to the *d*-band center theory, because of these effects, the downshifted Pt-weighted *d*-band center reduces the oxygen adsorption energy of Pt.[11−13] However, the TM used in this bimetallic alloy catalyst eventually leached out during the electrochemical reaction under acidic conditions. Continuous leaching of TM elements could lead to the loss of catalytic activity for two reasons: (1) reduction of the strain effect and ligand effect[14] and (2) sintering of Pt.[15] Thus, there has been

Received: August 2, 2023
Revised: September 23, 2023

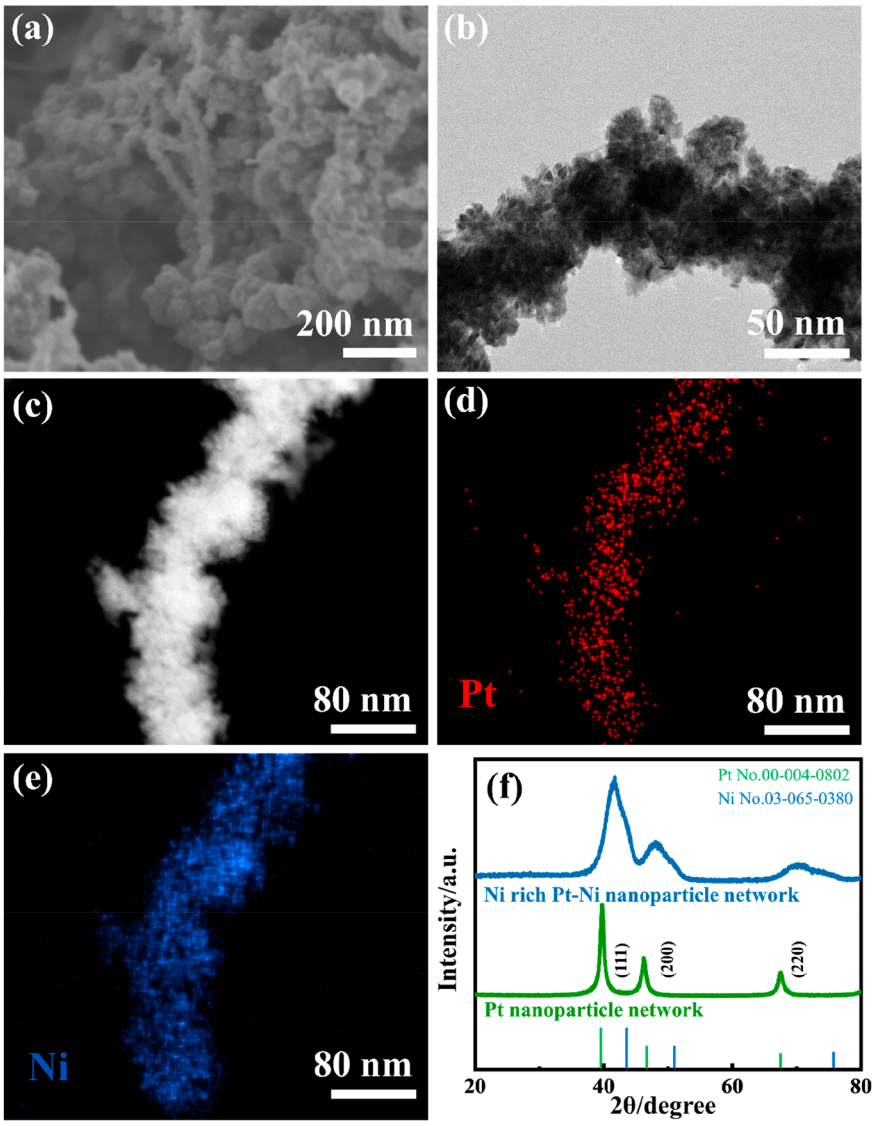

Figure 1. Morphological and compositional characterization of the Ni-rich Pt−Ni nanoparticle network catalysts. (a) Scanning electron microscopy (SEM) image of the Ni-rich Pt−Ni nanoparticle networks. (b) Transmission electron microscopy (TEM) image and (c) scanning transmission electron microscopy (STEM) image of the Ni-rich Pt−Ni nanoparticle networks. (d, e) Energy-dispersive X-ray spectroscopy (EDS) mapping images of Ni and Pt. (f) X-ray diffraction (XRD) patterns of the Pt nanoparticle networks and Ni-rich Pt−Ni nanoparticle networks.

an attempt to intentionally exploit the leaching phenomena of guest TMs in an electrochemical environment to further improve the activity and stability of Pt-based ORR electrocatalysts.[16−18] Li et al. fabricated jagged Pt nanowires (NWs) via electrochemical dealloying of PtNi alloy NWs.[18] They performed iterative cyclic voltammetry (CV) to dissolve the Ni atoms from the PtNi alloy NWs, which effectively increased their electrochemically active surface area (ECSA). Ding et al. fabricated 3D Pt−Ni network catalysts with nanoparticle intraporosity after controlled electrochemical dealloying using iterative CV, similar to the process reported by Li et al.[19] Compared to commercial Pt/C, these morphology-controlled Pt−Ni alloys via electrochemical dealloying showed excellent Pt mass activity and a large ECSA. Recently, the dealloying of Pt alloys with a high TM ratio has also been reported. In contrast to Pt-rich catalysts, Mani et al. fabricated Pt bimetallic nanoparticles with a high ratio of several TMs (Co, Cu, and Ni) and dealloyed them with electrochemical cycling.[20] Compared with Pt-rich precursors, TM-rich precursors can demonstrate substantial removal of the less noble component from the bulk of the catalysts, resulting in a severe rearrangement of the Pt surface and bulk atoms. Therefore, it can be confirmed that electrochemical dealloying of TM-rich alloys is a very effective strategy for controlling the morphology and activity of Pt−Ni alloys by the atomic rearrangement of the remaining components.[21,22]

The use of carbon supports for Pt catalysts has the disadvantage of driving carbon corrosion, which could cause an activity loss. Therefore, extensive efforts have been devoted to overcoming carbon corrosion: (1) corrosion-resistant supports, such as graphene, carbon nanotubes, Sb-SnO_2 and Ti_4O_7, and (2) supportless Pt catalysts.[23−25] However, the utilization of corrosion-resistant supports, which mitigate the carbon corrosion problem, is not effective for structural evolution, such as Pt redeposition, Ostwald ripening, and nanoparticle aggregation driven by surface energy minimiza-

https://doi.org/10.1021/acssuschemeng.3c04866
ACS Sustainable Chem. Eng. XXXX, XXX, XXX−XXX

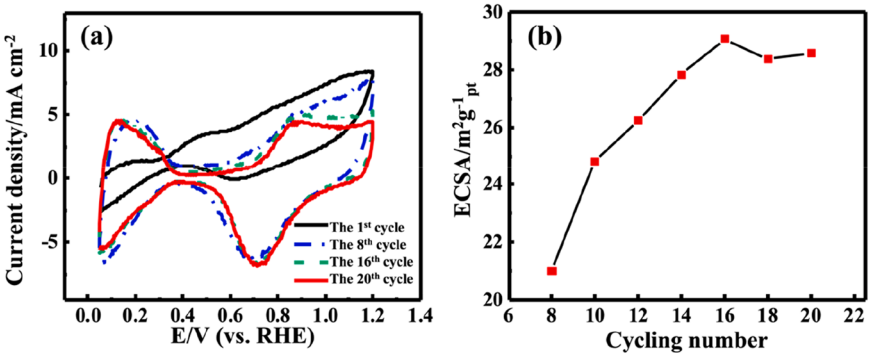

Figure 2. Cyclic voltammetry (CV) of the Ni-rich Pt−Ni nanoparticle networks conducted in an N_2-saturated 0.1 M $HClO_4$ electrolyte with a scan rate of 50 mV s^{-1}. (a) CV profiles of the Ni-rich Pt−Ni nanoparticle networks at cycle numbers of 1, 8, 16, and 20. (b) Electrochemically active surface area (ECSA(H_{upd})) variation as a function of cycle number.

tion.[26,27] Thus, a supportless Pt catalyst is the best strategy because it excludes support corrosion. The supportless Pt−Ni catalysts exhibited enhanced activity and durability compared to Pt/C.[28] However, supportless catalysts such as NWs and NP networks generally have lower mass activities than those of the supported catalysts. In order to overcome those limitations, dealloying strategies have been suggested for improving the electrocatalytic mass activity of Pt−Ni supportless catalysts. Wittkopf et al. fabricated supportless PtCu/Cu NW with enhanced activities through geometric lattice tuning by electrochemical dealloying.[29] This clearly shows that a supportless catalyst can be an excellent alternative for not only preventing carbon corrosion but also enhancing the specific and mass activities by electrochemical dealloying of TMs.

Based on the above two concepts, in this study, we synthesized dealloyed Pt−Ni nanoparticle networks with an enlarged ECSA and mass activity by a facile and robust electrochemical dealloying process. Supportless features of the dealloyed Pt−Ni nanoparticle could be able to prevent carbon corrosion and enhance specific and mass activities. Additionally, the unique nanoparticle structure of the dealloyed Pt−Ni could compensate for the structural instability during dissolution of Ni. We utilized both experimental methods and computational methods to analyze the physical and chemical aspects of the performance enhancement in our support-free catalyst. It was confirmed that the ECSA increased as the dealloying cycle number increased, leading to an abundance of active sites on the catalyst. We also performed density functional theory (DFT) calculations to elucidate the relationship between the catalytic activity and the effects of Ni (strain and ligand) on the dealloyed Pt−Ni nanoparticle network. Overall, the enlarged ECSA and alloy of PtNi allowed the dealloyed Pt−Ni nanoparticle to have high mass activity and stability, which could be made more sustainable and environmentally friendly catalysts by reducing the amount of Pt used and increasing the efficiency of the electrocatalysts.

RESULTS AND DISCUSSION

Physical Characterization of the Ni-Rich Pt−Ni Nanoparticle Networks. We utilized a modified solvothermal method to synthesize Ni-rich Pt−Ni nanoparticle networks using $Ni(acac)_2$ as the Ni precursor. Briefly, a mixed solution, in which KOH was added to EG and DMF, was used for the solvothermal synthesis. Hexachloroplatinic acid hexahydrate ($H_2PtCl_6{\cdot}6H_2O$) was dissolved in the mixed solution to form the precursor solution, which was then transferred into a Teflon-lined autoclave and maintained at 170 for 12 h (for more experimental details, please check the Supporting Information). The morphologies and elemental distributions of the produced Ni-rich Pt−Ni nanoparticle networks were revealed by SEM, TEM, and energy-dispersive X-ray spectroscopy (EDS) analyses. The SEM images (Figure 1a,b) revealed that the Ni-rich Pt−Ni nanoparticles were entangled and formed a network with a rugged surface on the microscale. In the tangled nanoparticle geometry, the nanoparticle assemblies are anchored to each other at multiple anchoring points, thereby impeding the movement of atoms, which is essential for the electrical and thermal stability of the nanoparticle networks.[18] The diameter of the Ni-rich Pt−Ni nanoparticle network was approximately 50 nm (Figure 1c), which was 10 nm thicker than that of the Pt nanoparticle bundles synthesized by the same process (Figure S1a−c).[19] Furthermore, Ni-rich Pt−Ni nanoparticle networks consist of agglomerated particles and exhibit significantly rough surfaces. We performed HAADF-STEM and EDS mapping to analyze the elemental distribution of the synthesized Ni-rich Pt−Ni nanoparticle networks (Figure 1d−f) and found that Pt and Ni were uniformly distributed throughout the nanoparticle networks. Moreover, the overall atomic ratio of Ni in the nanoparticle networks was 72.9 atom %, as measured by ICP-MS (Table S1a). This result confirmed that the nanoparticle networks were composed of a Ni-rich Pt−Ni alloy. Ni-rich Pt−Ni nanoparticle networks with rugged surface structures consisting of agglomerated particles were successfully obtained.

Next, we conducted XRD analysis on the Pt and Pt−Ni nanoparticle networks to demonstrate the changes in the lattice according to the alloying of the catalysts. Figure 1f shows the XRD patterns of the Ni-rich Pt−Ni and Pt nanoparticle networks. As shown in Figure 1f, both the Pt and Ni-rich Pt−Ni nanoparticle networks show clear diffraction peaks corresponding to the (111), (200), and (220) planes, indicating face-centered cubic (FCC) structures.[30] The diffraction peak positions of the Ni-rich Pt−Ni nanoparticle networks corresponding to the (111), (200), and (220) planes (2θ = 41.7°, 48.4°, and 69.7°) shifted to higher angles relative to those of the Pt nanoparticle networks (2θ = 39.8°, 46.2°, and 67.6°) by approximately 2°, indicating the formation of the Pt−Ni alloy.

Electrochemical Dealloying of the Ni-Rich Pt−Ni Nanoparticle Networks. To effectively increase the ECSA of the Ni-rich Pt−Ni nanoparticle networks, we conducted CV

https://doi.org/10.1021/acssuschemeng.3c04866
ACS Sustainable Chem. Eng. XXXX, XXX, XXX−XXX

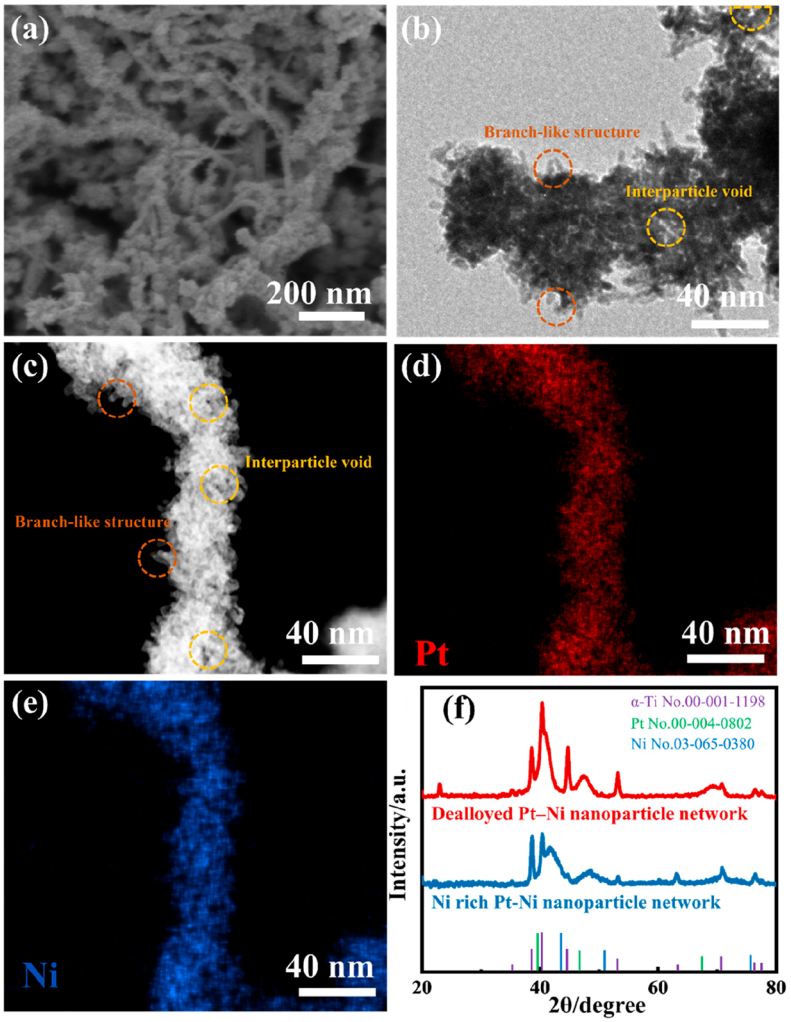

Figure 3. Morphological and compositional characterizations of the dealloyed Pt−Ni nanoparticle networks after 20 cyclic voltammetry (CV) cycles. Scanning electron microscopy (SEM) image of (a) the dealloyed Pt−Ni nanoparticle network. (b) Transmission electron microscopy (TEM) image and (c) scanning transmission electron microscopy (STEM) image of the dealloyed Pt−Ni nanoparticle networks (brown and yellow dotted circles indicate branch-like structures and interparticle holes, respectively). (d, e) 2D energy-dispersive X-ray spectroscopy (EDS) mapping images of Ni and Pt. (f) X-ray diffraction (XRD) patterns of the Ni-rich Pt−Ni nanoparticle networks and dealloyed Pt−Ni nanoparticle networks drop-casted on Ti film.

to electrochemically dissolve Ni. The CV dealloying of the Ni-rich Pt−Ni nanoparticle networks was conducted in a N_2-saturated 0.1 M $HClO_4$ solution with an applied voltage between 0.05 and 1.2 V vs RHE at a scan rate of 50 mV s^{-1} for 20 cycles. Figure 2 shows the sequential changes observed in the CV curve and ECSA (H_{upd}, underpotentially adsorbed hydrogen) as the number of cycles increased. At the first CV cycle, an oxidation peak appeared between 0.4 and 0.6 V, indicating the dissolution of Ni from the surface of the Pt−Ni nanoparticle networks (Figure 2a).[31] A hydrogen desorption/absorption peak between 0.05 and 0.4 V barely appeared in the first cycle, which was ascribed to the high concentration of Ni atoms at the surface, as shown in the XPS survey results (Table S1c). The Ni dissolution peak disappeared in the following CV cycles as the Ni atoms were gradually dissolved, whereas the hydrogen desorption/absorption peaks started to appear at the sixth cycle, indicating the exposure of Pt atoms on the surface.[32] The increase in the hydrogen desorption/absorption peak intensity reached a maximum at the 20th cycle and then saturated with further cycling. This saturation can be attributed to the leaching of a sufficient number of Ni atoms and the enrichment of the Pt atoms on the surface. The active sites of Pt obtained by the adsorption of hydrogenated species depending on the CV cycle are shown in Figure 2b (ECSA(H_{upd})). The ECSA(H_{upd}) is the integrated charge represented by the hydrogen peak intensity in the CV area (with double-layer charge subtracted) per unit charge required to oxidize the hydrogen monolayer on Pt and Pt loading on the electrode. As dealloying progressed, ECSA(H_{upd}) gradually increased and then saturated after the 16th cycle. Leaching of Ni atoms from the surface of the Ni-rich Pt−Ni nanoparticle networks increased the ECSA(H_{upd}), indicating an increase in the number of active Pt sites. The surface composition of the Pt−Ni nanoparticle networks, during the electrochemical dealloying process, changed from "Ni shell" to "Pt−Ni alloy" to "Pt-rich shell", as indicated by the changes in the CV curves. Increased surface area before and after dealloying also was confirmed by CO stripping measurement (ECSA(CO), Figure S2). The CO oxidation peak current density of the dealloyed Pt−Ni nanoparticle network (after dealloying) was signifi-

https://doi.org/10.1021/acssuschemeng.3c04866
ACS Sustainable Chem. Eng. XXXX, XXX, XXX−XXX

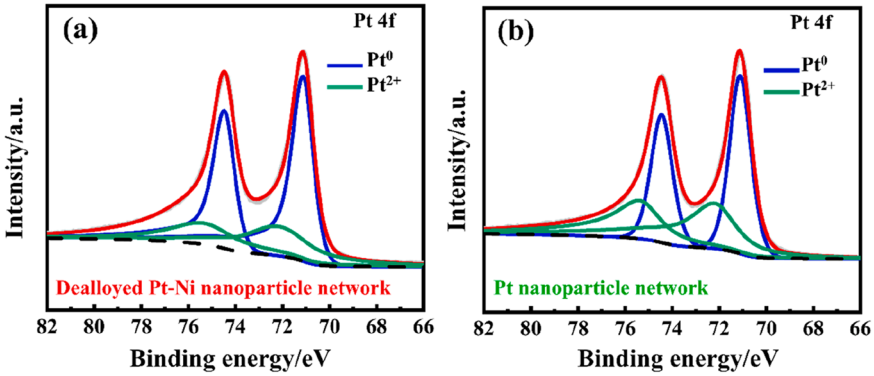

Figure 4. Pt 4f X-ray photoelectron spectroscopy (XPS) profiles of the (a) dealloyed Pt−Ni nanoparticle networks and (b) Pt nanoparticle networks, showing that the relative atomic ratio of Pt^0 to Pt^{2+} increases after dealloying.

cantly higher than that of the Pt−Ni nanoparticle network (before dealloying), indicating an increase in the active surface area. Moreover, both the onset and peak potentials of the dealloyed Pt−Ni nanoparticle networks were shifted to lower potentials than that of Pt/C. This negative potential shift indicates the downshift of the d-band center of the surface Pt. The lower potential for the oxidation of adsorbed CO on a Pt surface is due to weaker interaction between the Pt surface atoms and CO resulting from the modified electronic structures.[33,34] Furthermore, the ratios of ECSA(CO)/ECSA-(H_{upd}) were calculated to be 1.86 for Pt−Ni nanoparticle networks and 0.87 for Pt/C. This result corresponds to the previous reports, which demonstrated that the adsorption energy of hydrogen decreases when Pt skin and alloy are formed, leading to an increase in the ratio of CO to H.[35,36] These results confirm that we successfully increased the number of Pt active sites in the Pt−Ni nanoparticle networks via Ni dissolution and our previous claim of the formation of the PtNi alloy and Pt skin, assisted by iterative CV dealloying cycles and the CO stripping measurement.

Characterization of the Dealloyed Pt−Ni Nanoparticle Networks. The dissolution of Ni from the surface of the Pt−Ni nanoparticle networks by CV cycling revealed changes in the number of surface-active sites. The CV-induced changes in the morphology of the dealloyed Pt−Ni alloy were confirmed by SEM, TEM, and STEM-EDS analyses (Figure 3). The SEM images show that the network morphology of the nanoparticles was maintained even after the dissolution of Ni (Figure 3a,b). Moreover, compared with the Ni-rich Pt−Ni nanoparticle networks, the network of dealloyed Pt−Ni nanoparticles possessed a roughened surface with branch-like structures. TEM and STEM analyses were conducted to further evaluate the nanoscale morphology of the Pt−Ni nanoparticle networks (Figure 3c,d). Evidently, the nanoparticle networks exhibited rugged surfaces with branch-like and porous structures, and the diameter of the nanoparticle networks decreased from 50 nm (before dealloying) to ∼40 nm after the iterative CV-assisted dissolution of Ni. Furthermore, the EDS maps revealed that Pt and Ni atoms were uniformly distributed throughout the nanoparticle networks (Figure 3e,f). The dealloyed Pt−Ni nanoparticle networks were composed of nanosized agglomerates with interparticle voids and nanobranches at the surface. These interparticle voids and branches contribute to the 3D open-pore structure of the Pt−Ni nanoparticle networks and increase the number of Pt active sites. We also confirmed the atomic ratio of the dealloyed Pt−Ni nanoparticle networks from EDS spectral data. The atomic ratio of the dealloyed Pt−Ni nanoparticle network was 75.2:24.8 (at.%, Figure S3b) for Pt:Ni, which was considerably different from that of the Ni-rich Pt−Ni nanoparticle. These results show that Ni dissolution occurred during the iterative CV cycles, consistent with the increase in the ECSA, as the number of cycles increased after electrochemical dealloying. Moreover, the increase in the Pt atomic ratio indicated an increase in the Pt concentration on the surface, which is in agreement with the appearance of a strongly intense hydrogen desorption/adsorption peak at the 20th cycle. These results indicated that we successfully fabricated the dealloyed Pt−Ni nanoparticle networks with 3D open-pore branch-like surface structures composed of small particles and a Pt-rich surface.

To examine the changes in the lattice structures due to assisted dealloying of the Ni-rich Pt−Ni nanoparticle networks, we drop-cast the Ni-rich Pt−Ni nanoparticle networks on a Ti film and performed XRD analysis before and after dealloying (Figure 3f). After the CV cycle dealloying, the diffraction peaks of the dealloyed Pt−Ni nanoparticle networks appeared at 40.7°, 47.5°, and 68.9°, which can be assigned to the (111), (200), and (220) planes of the FCC phase of Pt. Evidently, these diffraction peaks appeared at angles lower than those of the Ni-rich Pt−Ni nanoparticle networks (2θ = 41.7°, 48.4°, 69.7°) before dealloying by approximately 1°. This peak shift can be ascribed to the dissolution of Ni during CV cycling, which changes the catalyst from a Ni-rich alloy to a Pt-rich one. The surrounding peaks, which appeared at 35.4°, 38.6°, 40.4°, 53.2°, 63.1°, 70.8°, 76.5°, and 77.5°, originated from the Ti film and were assigned to the (100), (002), (101), (102), (110), (103), (112), and (201) planes of the Ti film, respectively. These results indicate that the diffraction peaks of the dealloyed Pt−Ni nanoparticle networks appear at angles higher than those of the Pt nanoparticle networks. The larger diffraction peak shift observed after alloying resulted from compressive strain, which originated from the size difference between the atoms. The smaller Ni atoms generated compressive strain and possibly caused a downshift of the *d*-band center. This phenomenon may further weaken the adsorption strength of the adsorption of O, resulting in an improved ORR electrochemical activity (strain effect). Thus, the XRD analysis results confirmed the formation of a Pt−Ni alloy, as well as the dealloying of the Ni-rich Pt−Ni nanoparticle networks, indicating an expected enhancement in the ORR electrocatalytic activity of the Pt−Ni alloy.

https://doi.org/10.1021/acssuschemeng.3c04866
ACS Sustainable Chem. Eng. XXXX, XXX, XXX−XXX

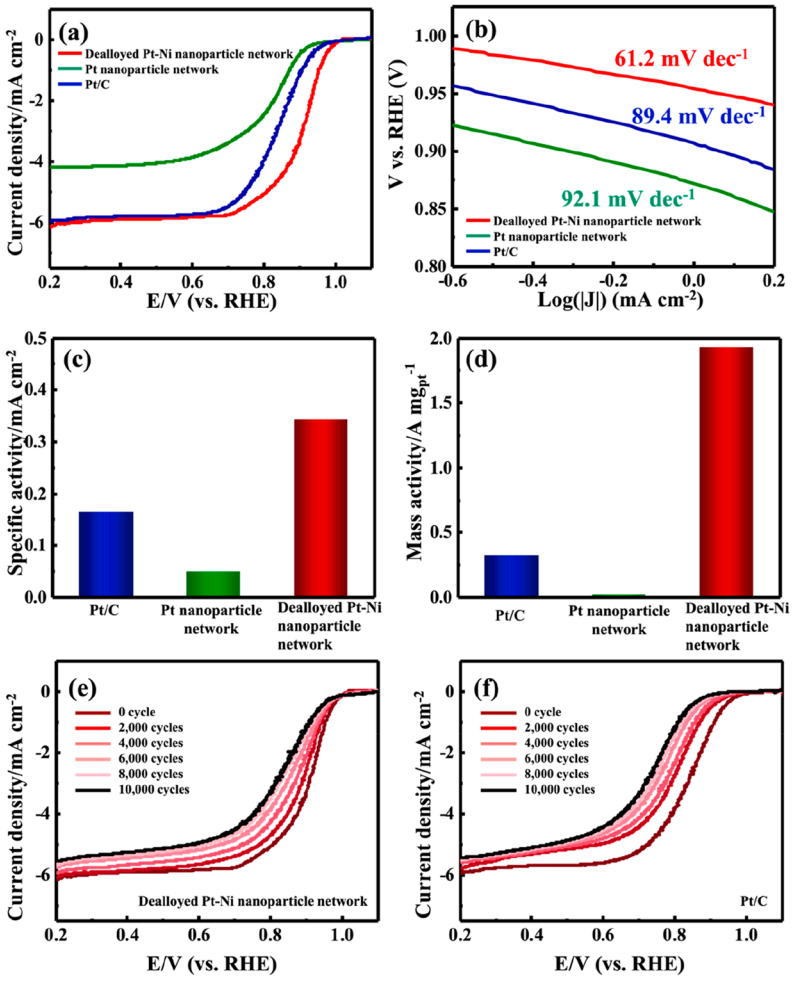

Figure 5. Electrocatalytic performance of the catalysts, i.e., the dealloyed Pt−Ni nanoparticle networks, Pt nanoparticle networks, and Pt/C. (a) LSV curves of Pt/C, Pt nanoparticle networks, and dealloyed Pt−Ni nanoparticle networks measured in an O_2-saturated 0.1 M $HClO_4$ electrolyte with a scan rate of 10 mV s^{-1}. (b) Tafel plots. (c) Specific and (d) mass activity estimated from the LSV curves obtained at 0.9 V vs RHE. LSV and 10000 cycles of ADT results of (e) the dealloyed Pt−Ni nanoparticle network and that of (f) Pt/C measured in an O_2-saturated 0.1 M $HClO_4$ electrolyte with a scan rate of 100 mV s^{-1}.

We further analyzed the chemical states and surface elemental compositions of the dealloyed Pt−Ni nanoparticle networks through X-ray photoelectron spectroscopy (XPS) analysis. Figure 4a and b show the Pt 4f XPS profiles of the dealloyed Pt−Ni and pure Pt nanoparticle networks, respectively. The Pt $4f_{7/2}$ signals can be divided into two peaks, which are assigned to Pt^0 and Pt^{2+}.[37] Quantitative analysis of the Pt^0 and Pt^{2+} peaks revealed that the dealloyed Pt−Ni nanoparticle networks contained a higher Pt^0 composition than did the Pt nanoparticle networks (Table S1(b)). The Pt^{2+} concentration was reduced by charge transfer from Ni to Pt, owing to the difference between the electronegativities of Pt and Ni.[38] The charge transfer from Ni to Pt, resulting in weak oxygen adsorption on the Pt surface, enhances the ORR performance. Moreover, we confirmed surface compositional changes in the Pt−Ni nanoparticle networks before and after dealloying. As presented in Table S1c, the Pt−Ni nanoparticle networks exhibited a high Ni atomic ratio before dealloying (Pt:Ni = 4:96). However, after dealloying, the atomic composition of Ni decreased significantly to 11 atom %, indicating that a large amount of Ni was dissolved from the surface of the Pt−Ni nanoparticle networks, leading to the observed surface compositional change from Ni rich to Pt rich. Interestingly, the atomic ratio of the dealloyed Pt−Ni nanoparticle networks obtained by XPS analysis was different from that obtained by EDS mapping analysis. This difference in the atomic ratios originates from the difference in penetration depth between the XPS and EDS techniques. The XPS method, with a low penetration depth, showed a more surface-sensitive elemental composition in comparison to the EDS method. Thus, XPS measurements confirmed that the dealloyed Pt−Ni nanoparticle networks had a lower Ni ratio at the surface than in the bulk (~30 at. %). These results validate the chemical state (reduced Pt) and surface elemental composition (lower Ni ratio at the surface than that in the bulk) of the dealloyed Pt−Ni nanoparticle networks.

Electrochemical Characterization of the Catalysts. Figure 5a shows the anodic-scan LSV results for the dealloyed Pt−Ni nanoparticle networks, Pt nanoparticle networks, and commercial Pt/C. The LSV scans were performed in an O_2-saturated 0.1 M $HClO_4$ electrolyte with an applied voltage between 0.2 to 1.1 V and a rotating speed of 1600 rpm with scan rate of 10 mV s^{-1}. First, we compared the dealloyed Pt−Ni nanoparticle networks with the Pt nanoparticle networks

https://doi.org/10.1021/acssuschemeng.3c04866
ACS Sustainable Chem. Eng. XXXX, XXX, XXX−XXX

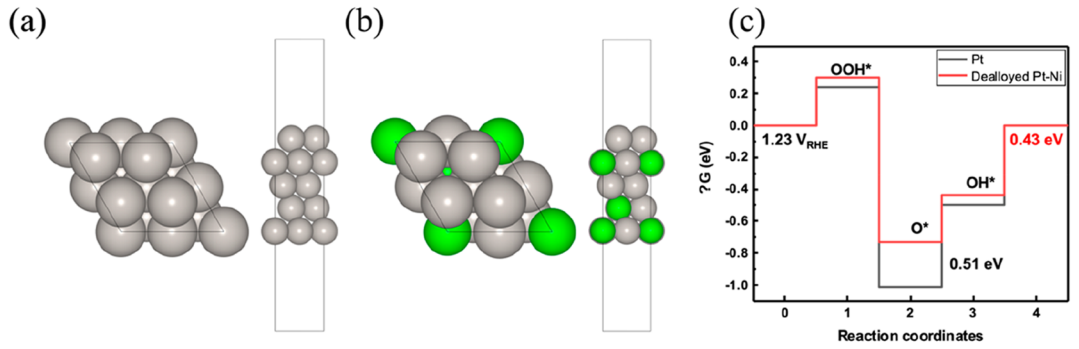

Figure 6. Model of (a) Pt(111) and (b) dealloyed Pt−Ni. The gray balls denote Pt atoms, and the green balls represent Ni atoms. (c) DFT-calculated Gibbs free energy diagrams indicating the ORR activities of Pt and dealloyed Pt−Ni at 1.23 V vs RHE.

and the commercial Pt/C. In comparison to the LSV curves of the Pt nanoparticle networks and Pt/C, those of the dealloyed Pt−Ni nanoparticle networks showed a half-wave potential ($E_{1/2}$, 0.918 V) that was higher than that of the Pt nanoparticle networks (0.818 V) and the commercial Pt/C (0.838 V). The limiting currents of the dealloyed Pt−Ni nanoparticle networks, Pt nanoparticle networks, and commercial Pt/C were determined to be 6.15, 4.18, and 5.76 mAcm^{-2}, respectively. The ORR kinetics were quantitatively compared using Tafel plots (Figure 5b). The dealloyed Pt−Ni nanoparticle networks exhibited faster reaction kinetics, with a Tafel slope of 61.2 mV dec^{-1}, compared to those of the Pt nanoparticle networks (92.1 mV dec^{-1}) and commercial Pt/C (89.4 mV dec^{-1}). The mass activity and specific activity were calculated by normalizing the kinetic currents, estimated using the Koutecky−Levich equation (Supporting Information for more details), against the Pt loading on the electrode and Pt surface area (ECSA(H_{upd})). The specific and mass activities of the catalysts obtained at a potential of 0.9 V are shown in Figure 5c,d. The dealloyed Pt−Ni nanoparticle networks exhibited the highest specific activity (0.343 mA cm^{-2}), which was higher than that of Pt/C (0.051 mA cm^{-2}) and that of the Pt nanoparticle networks (0.166 mA cm^{-2}). This result indicates that increasing the active surface area of the porous microstructure by CV dealloying results in the highest specific activity of the dealloyed Pt−Ni nanoparticle networks. The dealloyed Pt−Ni nanoparticle networks also showed the highest mass activity (1.93 A mg_{pt}^{-1}) at 0.9 V, and this mass activity was 6-fold higher than that of Pt/C (0.327 A mg_{pt}^{-1}) and also higher than that of the Pt nanoparticle networks (0.022 A mg_{pt}^{-1}). This trend is comparable to previous findings for dealloyed catalysts that contain Pt, as demonstrated in Figure S4, indicating that the dealloyed Pt−Ni nanoparticle networks performs efficiently as an ORR catalyst. All electrochemical measurement data and calculation information are listed in Table S2. Improvement in the electrocatalytic activity of the dealloyed Pt−Ni nanoparticle networks over that of pure Pt is attributed to the *d*-band downshift caused by the combined ligand and strain effects, as well as to the structural characteristic of high ECSA confirmed through the previously mentioned analyses. Therefore, because of the microporous structure realized by CV dealloying and the Ni-alloy effect, the dealloyed Pt−Ni nanoparticle networks exhibited a higher ORR performance than that of the Pt nanoparticle networks and commercial Pt/C.

Furthermore, the long-term durability of the electrocatalyst is crucial for achieving stable ORR performance. An ADT was performed to evaluate the durability of the catalyst by applying periodic potential sweeps from 0.6 to 1.1 V (vs RHE) at a scan rate of 100 mV s^{-1} in an O_2-saturated 0.1 M $HClO_4$ electrolyte with a rotation rate of 1600 rpm. The LSVs of the dealloyed Pt−Ni nanoparticle networks and Pt/C from 0 to 10000 potential cycles are shown in Figure 5e,f. Evidently, the dealloyed Pt−Ni nanoparticle networks showed a slightly changed half-wave potential and limiting current during 2,000 ADT cycles, indicating a loss of approximately 20 mV in the half-wave potential. In contrast, the commercial Pt/C showed a rapidly declining half-wave potential during the 2000 ADT cycles and a continuously decreasing half-wave potential over 10000 potential cycles. During the ADT, Pt/C demonstrated more significant degradation in both half-wave potentials, which is attributed to carbon corrosion. On the other hand, in the case of the dealloyed Pt−Ni nanoparticle networks, supportless nature can resolve this issue. To evaluate the improvement in stability, the morphology of the dealloyed Pt−Ni nanoparticle networks was confirmed by STEM and EDS mapping after the durability test (Figure S3c). The images showed that the dealloyed Pt−Ni nanoparticle networks maintained their network structure even after 10000 cycles. This result is in agreement with our previous results, suggesting that Ni leaching and the subsequent increase in the Pt concentration enhanced the ORR activity of the dealloyed Pt−Ni nanoparticle networks.

DFT Calculations. To theoretically elucidate the observed improved activity of the dealloyed Pt−Ni nanoparticle networks, we analyzed the ORR mechanism using DFT calculations. The Pt and dealloyed Pt−Ni nanoparticle networks were modeled, as shown in Figure 6a,b. The structural model of the Pt−Ni alloy, featuring an armored Pt skin that forms due to the dissolution of Ni on the surface, is widely recognized. This model explains that the high stability of the Pt−Ni alloy is maintained by the Pt skin, which prevents the dissolution of Ni in the core.[33] Five Pt layers, where each layer is considered a slab of the (111) plane with dimensions of 2 × 2, were modeled by assuming that the ORR proceeded on the plane with the lowest surface energy. In the dealloyed Pt−Ni model, we described a Pt_3Ni bulk part and a dealloyed Pt−Ni part. The bottom three layers depict the Pt_3Ni bulk, and the top two layers depict dealloyed Pt−Ni and Ni-dissolved Pt skin. This model is consistent with the experimentally confirmed Pt:Ni ratio at the surface and in the bulk (by XPS and EDS analyses, respectively) and ensures the reliability of the modeled slab.

https://doi.org/10.1021/acssuschemeng.3c04866
ACS Sustainable Chem. Eng. XXXX, XXX, XXX−XXX

The ORR mechanism was analyzed on the modeled slabs, and a Gibbs free energy diagram (GFD) was plotted, as shown in Figure 6c. The details of the formulas used to calculate the overpotential and GFD are described in the Supporting Information. The OH* generation step ($O^* + H^+ + e^- \rightarrow OH^*$) and the OH desorption step ($OH^* + H^+ + e^- \rightarrow H_2O^{+*}$) are the rate-determining steps (RDSs) of the ORR on the Pt(111) and dealloyed Pt−Ni surfaces, respectively. The calculated thermodynamic overpotential of the dealloyed Pt−Ni was found to be 0.43 V, which was lower than that of Pt (0.51 V) by 0.08 V. Because the reaction rate increases exponentially with decreasing overpotential, this result indicates that the dealloyed Pt−Ni exhibits a significantly higher catalytic activity than does Pt, and it is consistent with the catalytic-activity improvement trend observed in our experimental results.

Furthermore, we explored the mechanism underlying the observed higher activity of dealloyed Pt−Ni in comparison to that of Pt in terms of ligand and strain effects. Compared with the Pt(111) plane, the surface Pt skin of the dealloyed Pt−Ni was compressed by 2.4% owing to the Ni atoms on the subsurface. We modeled a 2.4% compressed Pt(111) plane and compared it with the uncompressed Pt(111) plane and dealloyed Pt−Ni to analyze the ligand and strain effects. Next, we calculated the *d*-band center, charge transfer, ΔE_O, and ΔE_{OH} values, as shown in Table S3. These results confirmed that the *d*-band center of the 2.4% compressed Pt(111) plane was lowered by compressive strain compared to that of the uncompressed Pt(111) plane, and this phenomenon reduced ΔE_O and ΔE_{OH} (strain effect). In addition, a comparison between the 2.4% compressed Pt(111) plane and the dealloyed Pt−Ni showed that the *d*-band center of the dealloyed Pt−Ni was lower than that of the 2.4% compressed Pt(111) plane, owing to electron transfer from Ni to Pt. This lowering of the *d*-band center also reduces ΔE_O and ΔE_{OH} (ligand effect). Notably, ΔE_{OH} was less influenced by strain and ligand effects than ΔE_O. This result can be explained by the difference in the adsorption of the O and OH on the surface (O: 3-fold, OH: 1-fold). Thus, the large reduction in ΔE_O compared to that in ΔE_{OH}, owing to the strong ligand and strain effects, facilitated the OH* generation step ($O^* + H^+ + e^- \rightarrow OH^*$), which is the RDS of Pt(111), and improved the activity of the dealloyed Pt−Ni.

CONCLUSION

In this study, we designed dealloyed Pt−Ni nanoparticle networks with a large ECSA using a facile electrochemical dealloying process to increase their ORR mass activity. We investigated the morphological and compositional changes to confirm the effects of iterative electrochemical dealloying. Based on the results, we confirmed that the electrochemical dealloying of the Ni-rich Pt−Ni nanoparticle networks leached out the Ni atoms uniformly from the surface, leading to the formation of a Pt-rich surface as well as a roughened surface of the Pt−Ni nanoparticle networks. We also performed DFT calculations to elucidate the origin of the enhanced ORR performance of the dealloyed Pt−Ni nanoparticle networks. The strain and ligand effects of Ni reduce the adsorption energy of the reaction intermediates, resulting in an increased catalytic activity. Overall, we successfully obtained morphology-controlled Pt−Ni nanoparticle networks with a large ECSA using a simple electrochemical dealloying strategy and ascertained the relationship between the strain and ligand effects of Ni and the ORR catalytic activity. The results of this study provide a new horizon for designing TM-alloy catalysts with Pt-rich skin and an increased surface area for applications that require catalysts exhibiting high ORR activities.

ASSOCIATED CONTENT

Data Availability Statement

The data sets generated during the present study are available from the corresponding author upon reasonable request.

Supporting Information

The Supporting Information is available free of charge at https://pubs.acs.org/doi/10.1021/acssuschemeng.3c04866.

Experimental details; computational details; structural characterization of Pt nanoparticle networks; CO stripping experiments; EDS mapping data before and after ADT; Plot for recently reported ORR electrocatalysts mass activity versus Tafel slope; Atomic concentration ratio of the catalysts measured by ICP-MS and XPS; Summarized electrochemical ORR performance for this work; Summarized DFT calculation data of this work (PDF)

AUTHOR INFORMATION

Corresponding Authors

Changsoo Lee − *Hydrogen Research Department, Korea Institute of Energy Research (KIER), Yuseong-gu, Daejeon 34129, Republic of Korea*; Email: cs.lee@kier.re.kr

Hyuck Mo Lee − *Department of Materials Science and Engineering, KAIST, Yuseong-gu, Daejeon 34141, Republic of Korea*; orcid.org/0000-0003-4556-6692; Email: hmlee@kaist.ac.kr

Authors

Jaeyoung Yoo − *Department of Materials Science and Engineering, KAIST, Yuseong-gu, Daejeon 34141, Republic of Korea*; orcid.org/0000-0002-9351-2421

Youngtae Park − *Department of Materials Science and Engineering, KAIST, Yuseong-gu, Daejeon 34141, Republic of Korea; Hydrogen Research Department, Korea Institute of Energy Research (KIER), Yuseong-gu, Daejeon 34129, Republic of Korea*

Jungwoo Choi − *Department of Materials Science and Engineering, KAIST, Yuseong-gu, Daejeon 34141, Republic of Korea*; orcid.org/0000-0003-3988-6331

Jeonghan Roh − *Department of Materials Science and Engineering, KAIST, Yuseong-gu, Daejeon 34141, Republic of Korea*; orcid.org/0000-0003-4080-580X

Kihyun Shin − *Department of Materials Science and Engineering, Hanbat National University, Yuseong-gu, Daejeon 34158, Republic of Korea*; orcid.org/0000-0002-1748-8773

Hyun-Seok Cho − *Hydrogen Research Department, Korea Institute of Energy Research (KIER), Yuseong-gu, Daejeon 34129, Republic of Korea*; orcid.org/0000-0001-8356-4490

EunAe Cho − *Department of Materials Science and Engineering, KAIST, Yuseong-gu, Daejeon 34141, Republic of Korea*; orcid.org/0000-0002-2871-6903

Complete contact information is available at: https://pubs.acs.org/10.1021/acssuschemeng.3c04866

https://doi.org/10.1021/acssuschemeng.3c04866
ACS Sustainable Chem. Eng. XXXX, XXX, XXX−XXX

Author Contributions

#These authors contributed equally (J.Y. and Y.P.). The manuscript was written through contributions of all authors. All authors have given approval to the final version of the manuscript.

Funding

This work was supported by a National Research Foundation of Korea (NRF) grant funded by the Korean government (MSIT) (Nos. RS-2022-00165520 and 2022M3H4A3A01083536).

Notes

The authors declare no competing financial interest.

■ ABBREVIATIONS

ADT, accelerated durability test; CV, cyclic voltammetry; DFT, density functional theory; ECSA, electrochemically active surface area; EDS, energy-dispersive X-ray spectroscopy; HAADF-STEM, high-angle annular dark-field scanning transmission electron microscopy; ICP-OES, inductively coupled plasma optical emission spectroscopy; LSV, linear sweep voltammetry; NW, nanowire; ORR, oxygen reduction reaction; PEMFC, proton-exchange membrane fuel cell; SEM, scanning electron microscopy; TM, transition metal; XPS, X-ray photoelectron spectroscopy; XRD, X-ray diffraction

■ REFERENCES

(1) Debe, M. K. Electrocatalyst approaches and challenges for automotive fuel cells. *Nature* **2012**, *486* (7401), 43−51.

(2) Li, M.; Zhao, Z.; Xia, Z.; Yang, Y.; Luo, M.; Huang, Y.; Sun, Y.; Chao, Y.; Yang, W.; Yang, W.; et al. Lavender-like Ga-doped Pt_3Co nanowires for highly stable and active electrocatalysis. *ACS Catal.* **2020**, *10* (5), 3018−3026.

(3) Liu, Q.; Du, L.; Fu, G.; Cui, Z.; Li, Y.; Dang, D.; Gao, X.; Zheng, Q.; Goodenough, J. B. Structurally ordered Fe_3Pt nanoparticles on robust nitride support as a high performance catalyst for the oxygen reduction reaction. *Adv. Energy Mater.* **2019**, *9* (3), 1803040.

(4) Toda, T.; Igarashi, H.; Uchida, H.; Watanabe, M. Enhancement of the electroreduction of oxygen on Pt alloys with Fe, Ni, and Co. *J. Electrochem. Soc.* **1999**, *146* (10), 3750.

(5) Wang, Z.; Yao, X.; Kang, Y.; Miao, L.; Xia, D.; Gan, L. Structurally ordered low-Pt intermetallic electrocatalysts toward durably high oxygen reduction reaction activity. *Adv. Funct. Mater.* **2019**, *29* (35), 1902987.

(6) Liu, M.; Zhao, Z.; Duan, X.; Huang, Y. Nanoscale structure design for high-performance Pt-based ORR catalysts. *Adv. Mater.* **2019**, *31* (6), 1802234.

(7) Shao, M.; Odell, J. H.; Peles, A.; Su, D. The role of transition metals in the catalytic activity of Pt alloys: quantification of strain and ligand effects. *Chem. Commun.* **2014**, *50* (17), 2173−2176.

(8) Escaño, M. C.; Gyenge, E.; Nakanishi, H.; Kasai, H. Pt/Cr and Pt/Ni catalysts for oxygen reduction reaction: to alloy or not to alloy? *J. Nanosci. Nanotechnol.* **2011**, *11* (4), 2944−2951.

(9) Li, J.; Li, L.; Wang, M. J.; Wang, J.; Wei, Z. Alloys with Pt-skin or Pt-rich surface for electrocatalysis. *Current opinion in chemical engineering* **2018**, *20*, 60−67.

(10) Luo, M.; Guo, S. Strain-controlled electrocatalysis on multimetallic nanomaterials. *Nature Reviews Materials* **2017**, *2* (11), 1−13.

(11) Nørskov, J. K.; Abild-Pedersen, F.; Studt, F.; Bligaard, T. Density functional theory in surface chemistry and catalysis. *Proc. Natl. Acad. Sci. U. S. A.* **2011**, *108* (3), 937−943.

(12) Bligaard, T.; Nørskov, J. K. Ligand effects in heterogeneous catalysis and electrochemistry. *Electrochim. Acta* **2007**, *52* (18), 5512−5516.

(13) Xiao, W.; Cordeiro, M. A. L.; Gong, M.; Han, L.; Wang, J.; Bian, C.; Zhu, J.; Xin, H. L.; Wang, D. Optimizing the ORR activity of Pd based nanocatalysts by tuning their strain and particle size. *Journal of Materials Chemistry A* **2017**, *5* (20), 9867−9872.

(14) Chattot, R.; Asset, T.; Bordet, P.; Drnec, J.; Dubau, L.; Maillard, F. Beyond strain and ligand effects: microstrain-induced enhancement of the oxygen reduction reaction kinetics on various PtNi/C nanostructures. *ACS Catal.* **2017**, *7* (1), 398−408.

(15) Plessow, P. N.; Abild-Pedersen, F. Sintering of Pt nanoparticles via volatile PtO_2: simulation and comparison with experiments. *ACS Catal.* **2016**, *6* (10), 7098−7108.

(16) Cui, C.; Gan, L.; Heggen, M.; Rudi, S.; Strasser, P. Compositional segregation in shaped Pt alloy nanoparticles and their structural behaviour during electrocatalysis. *Nature materials* **2013**, *12* (8), 765−771.

(17) Chen, C.; Kang, Y.; Huo, Z.; Zhu, Z.; Huang, W.; Xin, H. L.; Snyder, J. D.; Li, D.; Herron, J. A.; Mavrikakis, M.; et al. Highly crystalline multimetallic nanoframes with three-dimensional electrocatalytic surfaces. *Science* **2014**, *343* (6177), 1339−1343.

(18) Li, M.; Zhao, Z.; Cheng, T.; Fortunelli, A.; Chen, C.-Y.; Yu, R.; Zhang, Q.; Gu, L.; Merinov, B. V.; Lin, Z.; et al. Ultrafine jagged platinum nanowires enable ultrahigh mass activity for the oxygen reduction reaction. *Science* **2016**, *354* (6318), 1414−1419.

(19) Ding, J.; Ji, S.; Wang, H.; Key, J.; Brett, D. J.; Wang, R. Nano-engineered intrapores in nanoparticles of PtNi networks for increased oxygen reduction reaction activity. *J. Power Sources* **2018**, *374*, 48−54.

(20) Mani, P.; Srivastava, R.; Strasser, P. Dealloyed binary PtM_3 (M= Cu, Co, Ni) and ternary $PtNi_3M$ (M= Cu, Co, Fe, Cr) electrocatalysts for the oxygen reduction reaction: Performance in polymer electrolyte membrane fuel cells. *J. Power Sources* **2011**, *196* (2), 666−673.

(21) Erlebacher, J.; Aziz, M. J.; Karma, A.; Dimitrov, N.; Sieradzki, K. Evolution of nanoporosity in dealloying. *Nature* **2001**, *410* (6827), 450−453.

(22) Rugolo, J.; Erlebacher, J.; Sieradzki, K. Length scales in alloy dissolution and measurement of absolute interfacial free energy. *Nature materials* **2006**, *5* (12), 946−949.

(23) Ghosh, A.; Basu, S.; Verma, A. Graphene and functionalized graphene supported platinum catalyst for PEMFC. *Fuel Cells* **2013**, *13* (3), 355−363.

(24) Tian, Z. Q.; Lim, S. H.; Poh, C. K.; Tang, Z.; Xia, Z.; Luo, Z.; Shen, P. K.; Chua, D.; Feng, Y. P.; Shen, Z.; Lin, J. A highly order-structured membrane electrode assembly with vertically aligned carbon nanotubes for ultra-low Pt loading PEM fuel cells. *Adv. Energy Mater.* **2011**, *1* (6), 1205−1214.

(25) Binninger, T.; Fabbri, E.; Kötz, R.; Schmidt, T. J. Determination of the electrochemically active surface area of metal-oxide supported platinum catalyst. *J. Electrochem. Soc.* **2014**, *161* (3), H121.

(26) Chen, Z.; Waje, M.; Li, W.; Yan, Y. Supportless Pt and PtPd nanotubes as electrocatalysts for oxygen-reduction reactions. *Angew. Chem., Int. Ed.* **2007**, *46* (22), 4060−4063.

(27) Muench, F. Metal nanotube/nanowire-based unsupported network electrocatalysts. *Catalysts* **2018**, *8* (12), 597.

(28) Dogan, D. C.; Cho, S.; Hwang, S.-M.; Kim, Y.-M.; Guim, H.; Yang, T.-H.; Park, S.-H.; Park, G.-G.; Yim, S.-D. Highly durable supportless Pt hollow spheres designed for enhanced oxygen transport in cathode catalyst layers of proton exchange membrane fuel cells. *ACS Appl. Mater. Interfaces* **2016**, *8* (41), 27730−27739.

(29) Wittkopf, J. A.; Zheng, J.; Yan, Y. High-performance dealloyed PtCu/CuNW oxygen reduction reaction catalyst for proton exchange membrane fuel cells. *ACS Catal.* **2014**, *4* (9), 3145−3151.

(30) García-Diéguez, M.; Finocchio, E.; Larrubia, M. Á.; Alemany, L. J.; Busca, G. Characterization of alumina-supported Pt, Ni and PtNi alloy catalysts for the dry reforming of methane. *J. Catal.* **2010**, *274* (1), 11−20.

(31) Elgrishi, N.; Rountree, K. J.; McCarthy, B. D.; Rountree, E. S.; Eisenhart, T. T.; Dempsey, J. L. A practical beginner's guide to cyclic voltammetry. *Journal of chemical education* **2018**, *95* (2), 197−206.

(32) Biegler, T.; Rand, D.; Woods, R. Limiting oxygen coverage on platinized platinum; relevance to determination of real platinum area

https://doi.org/10.1021/acssuschemeng.3c04866
ACS Sustainable Chem. Eng. XXXX, XXX, XXX−XXX

by hydrogen adsorption. *Journal of Electroanalytical Chemistry and Interfacial Electrochemistry* **1971**, *29* (2), 269−277.
(33) Lyu, X.; Jia, Y.; Mao, X.; Li, D.; Li, G.; Zhuang, L.; Wang, X.; Yang, D.; Wang, Q.; Du, A.; Yao, X. Gradient-Concentration Design of Stable Core-Shell Nanostructure for Acidic Oxygen Reduction Electrocatalysis. *Adv. Mater.* **2020**, *32* (32), 2003493.
(34) Feng, Q.; Wang, X.; Klingenhof, M.; Heggen, M.; Strasser, P. Low-Pt NiNC-Supported PtNi Nanoalloy Oxygen Reduction Reaction Electrocatalysts—In Situ Tracking of the Atomic Alloying Process. *Angew. Chem., Int. Ed.* **2022**, *61* (36), No. e202203728.
(35) Becknell, N.; Kang, Y.; Chen, C.; Resasco, J.; Kornienko, N.; Guo, J.; Markovic, N. M.; Somorjai, G. A.; Stamenkovic, V. R.; Yang, P. Atomic structure of Pt_3Ni nanoframe electrocatalysts by in situ X-ray absorption spectroscopy. *J. Am. Chem. Soc.* **2015**, *137* (50), 15817−15824.
(36) van der Vliet, D. F.; Wang, C.; Li, D.; Paulikas, A. P.; Greeley, J.; Rankin, R. B.; Strmcnik, D.; Tripkovic, D.; Markovic, N. M.; Stamenkovic, V. R. Unique electrochemical adsorption properties of Pt-Skin Surfaces. *Angew. Chem., Int. Ed.* **2012**, *51* (13), 3139−3142.
(37) Sarkar, A.; Manthiram, A. Synthesis of Pt@ Cu core- shell nanoparticles by galvanic displacement of Cu by Pt^{4+} ions and their application as electrocatalysts for oxygen reduction reaction in fuel cells. *J. Phys. Chem. C* **2010**, *114* (10), 4725−4732.
(38) Zhu, J.; Yang, Y.; Chen, L.; Xiao, W.; Liu, H.; Abruña, H. c. D.; Wang, D. Copper-induced formation of structurally ordered Pt-Fe-Cu ternary intermetallic electrocatalysts with tunable phase structure and improved stability. *Chem. Mater.* **2018**, *30* (17), 5987−5995.

https://doi.org/10.1021/acssuschemeng.3c04866
ACS Sustainable Chem. Eng. XXXX, XXX, XXX−XXX